

Polarized Neutron Measurements of the Internal Magnetization of a Ferrimagnet Across its Compensation Temperature

C. D. Hughes^{a,b,c}, K. N. Lopez^{a,b,c,*}, T. Mulkey^d, B. Hill^e, J. C. Long^e, M. Sarsour^d, M. Van Meter^{a,b,c}, S. Samie^{a,b,c}, D. V. Baxter^{a,b}, W. M. Snow^{a,b,c}, L. M. Lommel^f, M. Luxnat^{a,b,c}, Y. Zhang^g, C. Jiang^g, E. Stringfellow^g, P. Zolnierczuk^g, M. Frost^g, M. Odom^g

^aDepartment of Physics, Indiana University, 727 E. 3rd St., Bloomington, IN 47405, USA

^bCenter for Exploration of Energy and Matter, 2401 N. Milo B. Sampson Ln., Bloomington, IN 47408, USA

^cIndiana University Center for Spacetime Symmetries, 727 E. 3rd St., Bloomington, IN 47405, USA

^dDepartment of Physics and Astronomy, Georgia State University, Atlanta, GA 30303, USA

^eDepartment of Physics, University of Illinois at Urbana-Champaign, Urbana, IL 61801, USA

^fUniversity of Notre Dame, Holy Cross Dr., Notre Dame, IN 46556, USA

^gOak Ridge National Laboratory, Oak Ridge, TN 37830, USA

arXiv:2408.14794v2 [cond-mat.mtrl-sci] 11 Apr 2025

Abstract

We present the first polarized neutron transmission image of a model Néel ferrimagnetic material, polycrystalline terbium iron garnet ($\text{Tb}_3\text{Fe}_5\text{O}_{12}$, TbIG for short), as it is taken through its compensation temperature T_{comp} where the macroscopic magnetization vanishes. Our polarized neutron imaging data and the additional supporting measurements using neutron spin echo spectroscopy and SQUID magnetometry are all consistent with a vanishing internal magnetization at T_{comp} .

1. Introduction

Ferrimagnetic materials contain distinct sublattices of atoms with magnetic moments of different magnitudes and antiferromagnetic coupling among those atoms. The different moment size leads to a net magnetic moment at the unit cell level despite this antiferromagnetic coupling. In general, the temperature dependence of the sublattice magnetizations can be different, so it is possible for the magnetic moment per unit cell of the ferrimagnet to go to zero at a particular temperature that is known as the magnetic compensation temperature (T_{comp}). If the gyromagnetic ratios of the two atoms differ, the unit cell will also exhibit a non-zero total angular momentum \vec{J} at T_{comp} . Moreover, since the ratio of the orbital and spin components of the total angular momentum may also vary for different atoms, there can remain some nonzero total orbital angular momentum \vec{L} and a nonzero total spin angular momentum \vec{S} at T_{comp} as well. The total angular momentum ($\vec{J} = \vec{L} + \vec{S}$) may vanish at a different temperature $T_A \neq T_{comp}$.

The existence of ferrimagnetism has been known for several decades [57, 23, 13]. Textbooks and reviews on the phenomenon describe what is known experimentally, which consists mostly of measurements of the external magnetic field produced by the internal magnetization, and the theory of ferrimagnetism is thought to be reasonably well understood [7, 15, 14, 31, 32]. Recently, special

aspects of this phenomenon have attracted scientific attention from new directions. If a ferrimagnet possesses magnetic domains at T_A , for example, the fast domain-wall dynamics predicted for $\vec{J} = 0$ antiferromagnetic materials might occur instead in a material with a net magnetic moment, which in turn could enable these domains to be manipulated with external magnetic fields [39, 33]. In addition, a ferrimagnet at T_{comp} realizes a very interesting new type of polarized target medium: according to the simple model described above, it can be understood as an ensemble of polarized electrons with no net internal or external magnetic field.

Measurements characterizing ferrimagnetic phenomena have typically sensed the readily-accessible macroscopic external fields, and applications for these materials typically rely on the net moment. There has been relatively little detailed study of the microscopic magnetic structure of these materials at T_{comp} . For applications that rely on a net spin polarization at T_{comp} , there remains some concern that the simple mean-field description of the local spin structure could be complicated by disorder near domain walls and other deviations from the simplistic model of the macroscopic sample being a homogeneous periodic replication of ideal unit cells. These possibilities motivate a careful study of the internal magnetic structure of a ferrimagnetic material as it is taken through its magnetic compensation point.

In this paper we present to our knowledge the first images of the internal magnetization of a ferrimagnet taken through T_{comp} . With the advent of polarized neutron

*Corresponding author.

Email address: knlopez@iu.edu (K. N. Lopez)

imaging, one can measure the internal magnetic fields of a material using polarized neutron spin rotation in transmission.

The net electron spin polarization with no net magnetization of a compensated ferrimagnet at T_{comp} makes such systems an excellent choice to search for possible exotic spin-dependent interactions of electrons with matter without an overwhelming spin-dependent background signal from magnetic interactions. Such exotic spin-dependent interactions are predicted in a very wide variety of theories beyond the Standard Model of particles and interactions, including string theory [43, 73, 52, 16, 1, 34, 45, 53]. Experiments must be optimized for different regimes within the wide spectrum of possible interaction ranges. The range of these interactions is inversely proportional to the mass of the associated exchange boson. One spin-dependent exotic interaction search in preparation [45] uses a ferrimagnet attached to a mechanical oscillator with sensitivity at the thermal noise limit to investigate a wide variety of possible exotic spin-dependent interactions with macroscopic range. A recent review [65] and a book chapter [19] have placed this work in the context of analogous investigations using atomic measurements.

Slow neutrons are well-suited for such searches [56, 17, 61, 70, 69], and several sensitive neutron experiments have been conducted to constrain such interactions [40, 20, 6, 55, 66, 72, 63, 60, 35, 2, 44, 36, 11, 29, 75, 41, 46, 42, 26, 25, 59]. The ability of slow neutrons to move through matter with minimal quantum decoherence enables phase-sensitive interferometric measurement methods of various types. Efficient techniques to polarize and analyze neutron beams and manipulate the neutron spin are well-developed.

A sensitive experimental search for possible exotic spin-dependent interactions of polarized neutrons with polarized electrons can uncover new interactions of Nature inaccessible by other methods. For shorter range interactions, the number of spin-polarized particles that can be brought within the relevant interaction range simply by bringing two macroscopic objects close to each other becomes smaller and smaller. It also becomes more and more difficult to maintain the required control over systematic background effects from magnetic field distortions generated by test mass susceptibility and magnetic impurities. Spin-dependent interactions with short ranges inaccessible to measurements with macroscopic bodies can be searched for using coherent neutron transmission measurements. The neutron optical potential of the matter that the neutron passes through is sensitive to any contribution to the real part of the forward scattering amplitude. These contributions include any spin-dependent interactions and those from the exotic interaction of interest.

The number of possibilities for the form of such exotic interactions beyond the Standard Model of particles and interactions is not as arbitrary as one might suppose. Theoretical work on the possible interactions among point particles [16, 18] reveals 16 linearly-independent nonrela-

tivistic potentials from the single exchange of a spin-0 or spin-1 boson composed from scalar invariants involving the spins, momenta, interaction range, and possible particle couplings between nonrelativistic spin-1/2 fermions. Experimental laboratory constraints on the subset of these possible interactions involving two polarized species are scarce, especially for short-range interactions. “In-matter” gravitational torsional fields can be sourced by the polarized electron ensemble. Just as mass curves spacetime in general relativity, the other property that all matter particles possess in addition to mass, namely spin, has long been thought to produce an additional “twist” of spacetime, geometrically independent of curvature, called torsion [30, 68, 27]. To experimentally probe torsion effects at short distances [9] requires one to probe inside a dense system of polarized particles. Polarized neutron transmission through a magnetically-compensated ferrimagnet is one of the very few known systems in which one can perform such an experimental search.

To use a magnetically-compensated ferrimagnet to search for new interactions, it is essential to extract direct information of the actual magnetic fields inside the sample at T_{comp} . Previous work using polarized neutron scattering as an internal probe of ferrimagnetic materials [47, 8, 54] did not investigate the magnetic structure at T_{comp} . Polarized neutron imaging can directly measure the line integrals of the internal magnetic fields along the neutron trajectories using polarized neutron spin rotation. Neutron spin echo spectroscopy in transmission can achieve even higher sensitivity to internal fields, albeit with lower spatial resolution.

The remainder of this paper is organized as follows. Section 2 describes our sample fabrication and magnetization procedure. Section 3 summarizes our local characterization studies of TbIG ferrimagnetic samples using SQUID magnetometry and x-ray diffraction. Section 4 provides detail on our custom sample environment and temperature control system. Section 5 describes our results from the Spallation Neutron Source Neutron Spin Echo spectrometer at Oak Ridge National Laboratory (ORNL). Section 6 describes the neutron polarimeter setup on the High Flux Isotope Reactor (HFIR) neutron imaging beamline at ORNL, and Section 7 presents 2D images of the net polarized neutron spin rotation angle through the sample as a function of the sample temperature as it is taken through T_{comp} . These images clearly show the magnetization vanishing at T_{comp} and reversing sign above and below T_{comp} . We compare the magnetization inferred from this data with a mean field model of ferrimagnetism as applied to TbIG, and we also use this model to infer the polarized electron spin density at T_{comp} . We conclude with a description of ongoing data analysis of the polarized neutron images to learn about or constrain the possible presence of ferrimagnetic domains and to search for possible exotic spin-dependent interactions of polarized neutrons and polarized electrons.

1.1. Review of ferrimagnetism in TbIG

TbIG is an intermetallic compound with the magnetic properties of a ferrimagnet. Ferrimagnets exhibit spontaneous alignment of magnetic moments within domains like ferromagnets, but the resulting magnetization is low, since the magnetic moments of the sublattice species oppose each other. Here, the Tb lattice aligns with one Fe lattice and anti-aligns with another (see Sec. 7). The magnitudes $\mu_{Fe}(T)$ and $\mu_{Tb}(T)$ of the respective moments vary with temperature with a dependence that can be calculated in a mean-field model given sufficient knowledge of the various moment-moment couplings. The magnetic moment of the iron is mostly due to the spin of electrons, but that of the terbium has a significant contribution from the orbital motion of the inner shell 4f electrons.

The moment directions can possess a small canting angle θ_c determined by interatomic forces within the crystal. In this paper we will assume, consistent with our observations, that the canting angle θ_c , if present, is a fixed property of the crystal lattice, independent of temperature and applied magnetic field. As the data will show, we see no evidence for a net nonzero canting angle upon averaging over the sample volume.

2. Sample Fabrication and Magnetization

2.1. Fabrication

Our polycrystalline rare-earth iron garnet samples are produced using a coprecipitation method [74, 24, 4, 38]. Stoichiometric amounts of $\text{Re}(\text{NO}_3)_3$ and FeCl_3 are added to deionized water to create 1 molar (M) stock solutions, where Re is the rare earth element of choice. A 6 M solution of NaOH acts as the precipitating agent in the reaction, and the resulting solution containing the precipitant is brought to a neutral pH with a deionized water wash before being dried at 120° C for at least 12 hours. The dried material is subsequently calcined for at least 12 hours at 1200°C. The material is then ground, pressed, and fired again to increase the purity.

Powder samples of TbIG were fabricated from freshly synthesized material, pressed into cylindrical samples, and fired in a furnace up to temperatures of 1200°C. The resulting samples were 19 mm in diameter and 7.4 mm thick, with density 3.8 g/cm³.

2.2. Magnetization

Like a ferromagnet, a ferrimagnet is magnetized by exposing it to an external magnetic field intense enough to saturate the magnetization. In our case, this magnetization step was performed at room temperature. The cylindrical TbIG samples were magnetized along the longitudinal axis using a large NMR electromagnet capable of field strengths near 1 Tesla with fractional magnetic field uniformity of better than 10^{-4} over the sample volume. The accuracy of alignment of the external magnetic field direction and the axis of the sample was better than 1 mrad.

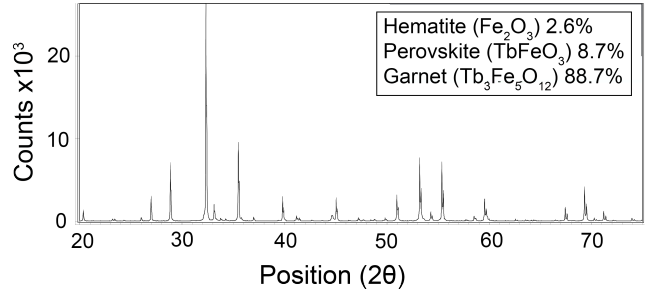


Figure 1: Measured X-ray intensity vs. 2θ angle. Diffraction pattern is typical of a terbium iron garnet, with additional peaks contributed by contaminants. Results of a Rietveld analysis of this TbIG sample are displayed in the upper right corner.

3. Sample Characterization

3.1. X-Ray Diffraction

We employed X-ray powder diffraction measurements to help tune the sample preparation process, minimizing the perovskite phase (TbFeO_3) and hematite (Fe_2O_3), the principal observed contaminants. Material was sequestered from the bulk before samples were pressed into pellets. The samples were then analyzed in a Bruker D8 Advance PXRD device using $\text{CuK}\alpha$ radiation at the Indiana University Molecular Structure Center. The resulting scans were compared to standards in either the Powder Diffraction File-2 (PDF-2) database or the Inorganic Crystal Structure Database (ICSD). A Rietveld refinement of the data was performed to determine composition fractions. Using this method, we determined the purity of sample Tb082422_f103 to be 88.7% $\text{Tb}_3\text{Fe}_5\text{O}_{12}$ (weighted residual profile value of 13.80% and a χ^2 goodness-of-fit of 4.65), with TbFeO_3 making up the majority of the remainder along with some contribution from Fe_2O_3 . Figure 1 shows the results of a Rietveld analysis of an optimized sample.

Both of the contaminants can, in principle, contribute to the magnetic signal. Based on our knowledge of their properties from previous scientific literature, we anticipated that they would not interfere with the interpretation of our experimental data. The orthoferrite TbFeO_3 is a weak antiferromagnet with anti-aligned but slightly canted magnetic moments [71]. The hematite Fe_2O_3 is a pure antiferromagnet under 260 K, but undergoes a Morin transition at 260 K into a weak antiferromagnet [3]. Antiferromagnetic ordering will not contribute to the experimental observables we employ, and we see no evidence for magnetic contributions from these sample contaminants in our data as will be clear below.

3.2. SQUID Magnetometry

We measured the external fields from TbIG and also dysprosium iron garnet (DyIG) samples using a Quantum Design MPMS-XL SQUID system to infer a compensation temperature of 229.5 ± 0.5 K for DyIG (Fig. 2) and

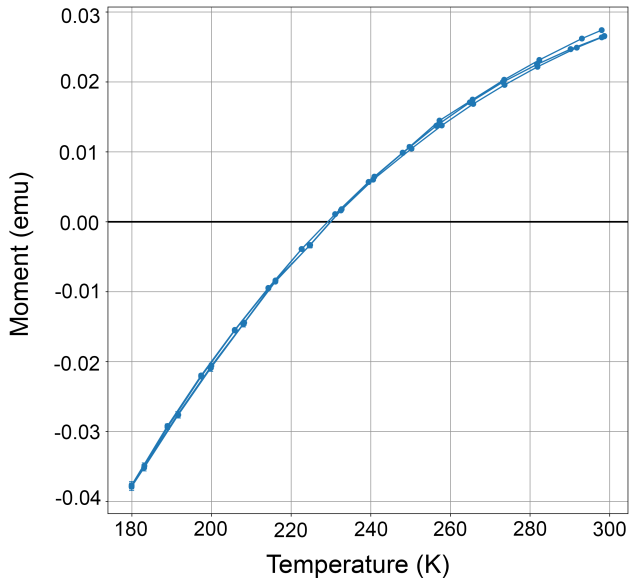


Figure 2: Total remanent magnetic moment (in zero applied field) of a small (0.32 cm diameter) DyIG sample as a function of temperature, as measured in MPMS magnetometer. Data are for several cycles of the temperature between 180 K and 298 K.

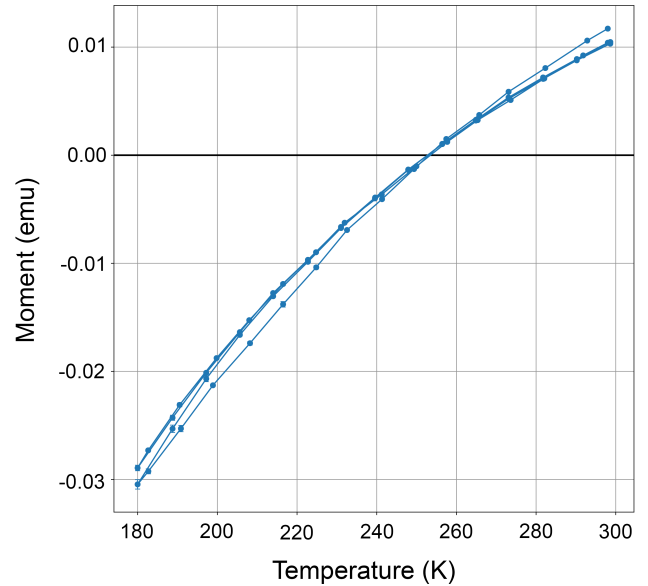


Figure 3: Total remanent magnetic moment (in zero applied field) of a 0.32 cm diameter TbIG sample as a function of temperature, as measured in the MPMS magnetometer. Data are for several cycles of the temperature between 180 K and 298 K. The slight variations between cycles, away from T_{comp} , are consistent with a small amount of sample motion from the limited rigidity of the sample mount.

253 ± 1 K for TbIG (Fig. 3). These compensation temperatures were reproducible under different sample preparation states and upon thermal cycling, and showed no evidence of hysteresis within measurement errors and instrumentation limitations.

4. Previous Neutron Work

Few neutron experiments involving TbIG have been performed. Some references to work from more than three decades ago exist [5, 49, 21, 22]. More abundant literature is available on yttrium iron garnets (YIG), a popular material used for many years in spintronic and microwave devices. Plant et al. [62] used unpolarized neutrons to explore the dispersion of spin wave excitations. More recent work using unpolarized [48, 67, 64] and polarized [54, 8] neutrons has been conducted to further explore spin waves, magnon polarization, and other magnetic properties in YIG. To our knowledge, none of the neutron measurements described below have been previously conducted on TbIG.

4.1. Sample Environment Design and Temperature Control for Polarized Neutron Measurements

The TbIG samples are held in a custom aluminum mount shown in Figure 4 which allows for two samples to be mounted simultaneously. Aluminum has a high thermal conductivity and also a relatively low neutron scattering and absorption cross section compared to TbIG. The mount allows for up to four silicon diode sensors to be attached for thermometry. The mount is secured to a copper disk at the end of a cold finger inside of a Cryo Industries Model RC102 sample-in-vacuum continuous flow cryogenic

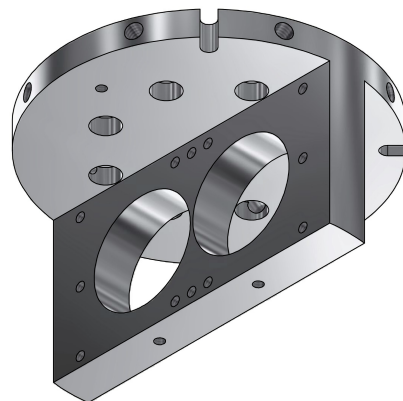


Figure 4: The two-cell sample holder used in the SNS-NSE experiment.

workstation. A thin aluminum radiation shield designed to minimize possible thermal gradients in the sample from nonuniform radiative heating attaches to the outer rim of the mounting disk. Three sapphire plates manufactured by Gavish Sapphire Products hold the samples in place. Sapphire was chosen for this purpose due to its low neutron absorption and scattering cross section and high thermal conductivity. One large sapphire plate remains flush with the sample mount such that the sample side of the plate, the edge of the sample mount, and the sample face are coplanar. The other face of the pellet is secured using a smaller sapphire plate, half the length of the large plate and the same width and thickness. This allows for samples of different thicknesses to be mounted in the two sample cells. Both sapphire plates were held in place with aluminum brackets and brass screws which were scanned for internal magnetic fields from magnetic impurities and found to have no fields larger than 50 nT a few mm away from the sensitive volume of a fluxgate magnetometer. To improve thermal contact area and thereby minimize thermal gradients in the sample, a small amount of Krytox grease was applied to the plate where it makes contact with the pellet. Krytox is a fluorinated grease chosen to avoid the strong neutron scattering that would arise from any grease composed of hydrogenous materials.

The body of the cryostat is made of aluminum with four windows on either side of the cubic base. The main vacuum windows of the cryostat were replaced with sapphire windows, also produced by Gavish. The original screws for the retaining ring of the cryostat windows were replaced with brass screws and washers scanned for magnetic impurities using fluxgate magnetometers. A rough vacuum is maintained within the volume of the cryostat using a dry scroll pump.

The cryogenic coolant is liquid nitrogen. The cryogen is allowed to flow into the cryostat at a rate controlled by the dewar pressure and conductance of the transfer line before boiling and venting to atmosphere. The temperature of the system is controlled via PID feedback loop using a Lakeshore Model 331 temperature controller, managed via a slow-control LabVIEW program, the silicon-diode temperature sensors, and a resistive heater embedded in the sample mount at the end of the coldhead. With this scheme, we are able to reliably achieve temperature stability of 100 mK.

5. Neutron Spin Echo Measurements

We used the Neutron Spin Echo spectrometer at Oak Ridge National Laboratory’s Spallation Neutron Source (SNS-NSE) to investigate the internal magnetization of TbIG as a function of temperature. In transmission mode, the NSE spectrometer can measure the line integral of the internal magnetic field of the sample along the neutron trajectories using the phase shift of the interference fringes of the neutron spin echo signal. NSE can also search for possible components of sample magnetization normal to

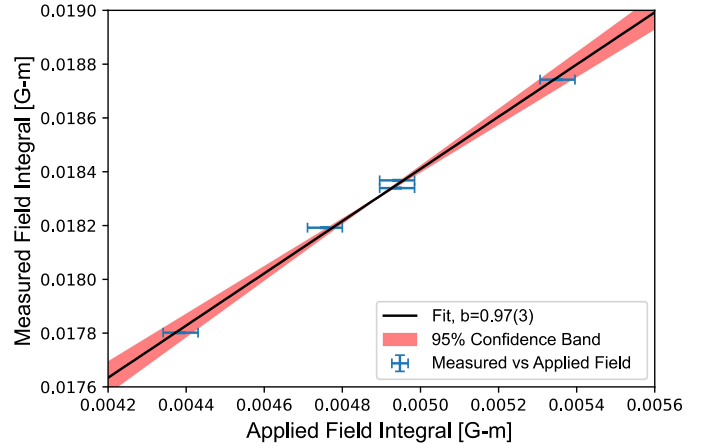


Figure 5: Calibration of the SNS Neutron Spin Echo instrument’s phase shift versus a known, applied magnetic field integral in the sample region as measured over a neutron wavelength range between 1.3 meV and 3.2 meV.

the neutron momentum transfer \vec{Q} by using the sample itself as the π flipper to generate the spin echo pattern (the so-called “paramagnetic” neutron spin echo mode) [51, 37, 58, 50, 10].

Before the measurement, we calibrated the response of the SNS neutron spin echo spectrometer in transmission mode to a known magnetic field integral applied in the sample region (Fig. 5). This measurement achieved a 100 nT-m field integral sensitivity in a half-hour of beam time with the SNS spallation target power at 1.5 MW.

Figure 6 shows the amplitude and phase shift of the neutron spin echo envelope in forward transmission when operated in paramagnetic mode, which uses the sample itself as the π -flipper to form the spin-echo. In this case the central point of the echo occurs at an interference minimum.

Figure 7 shows the centroid amplitude of the interference signal as a function of the temperature, with data points taken through both a heating and cooling cycle. This amplitude is that of the sinusoidal signal shown in the plots displaying intensity as a function of phase current (Fig. 6). These measurements are consistent with the previous SQUID measurements and the in-situ measurements made with Hall probes and fluxgate magnetometers, showing an amplitude which vanishes within the statistical accuracy of the measurements around $T = 250.3$ K.

Some data were also taken with the downstream arm of the spectrometer set to an angle of 4 deg relative to the incident neutron momentum. This latter setting corresponds to a range of momentum transfers Q between 0.062 \AA^{-1} and 0.088 \AA^{-1} for the incident neutron energies of 1.3 meV and 3.2 meV selected by the upstream neutron choppers. The direction of the neutron momentum transfer for this spectrometer setting lies in the horizontal plane and points nearly normal to the incident neutron momentum direction. Figure 8 shows the neutron spin echo signal at temperatures of 230K, 251K, and 270K.

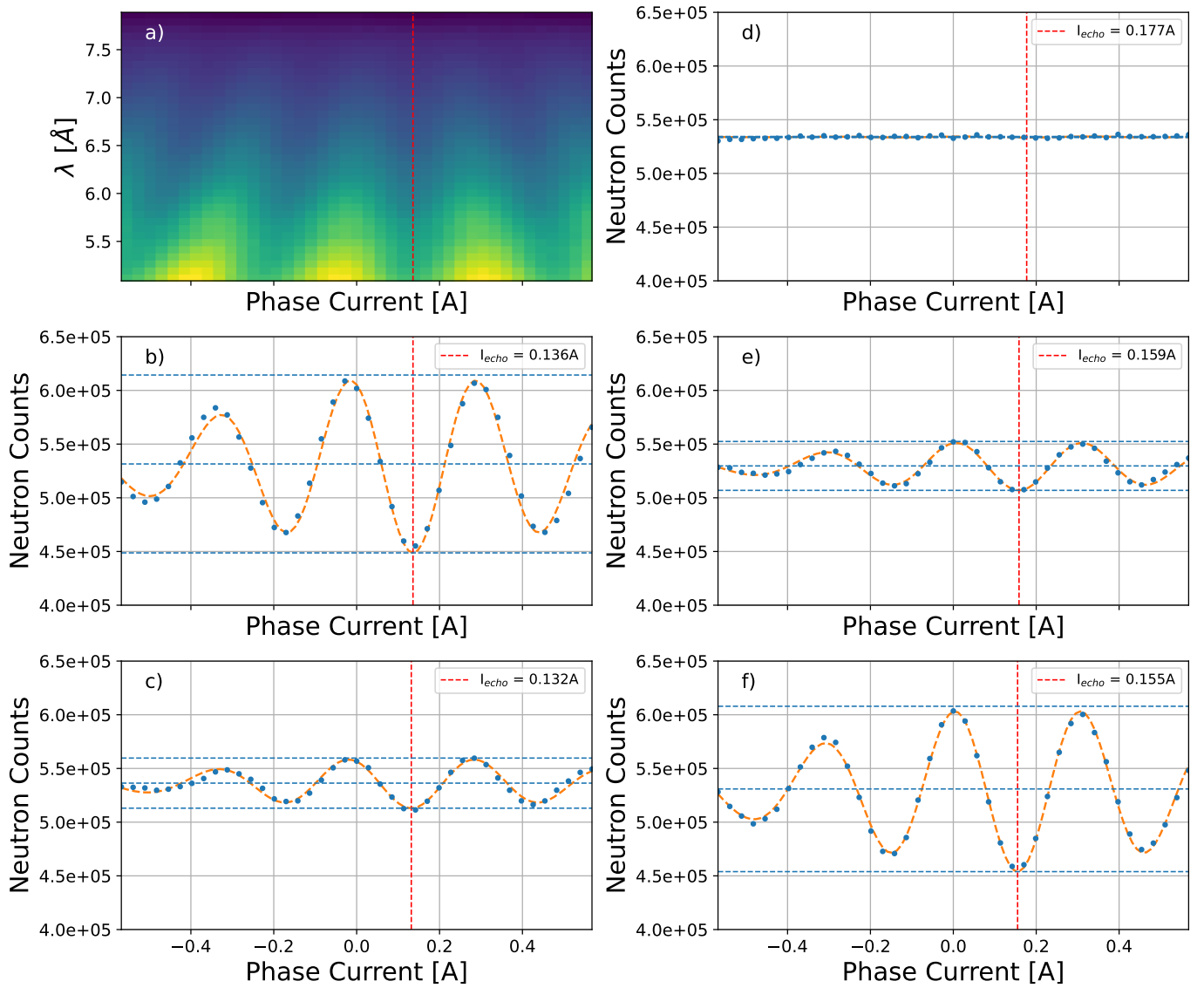


Figure 6: Plots of the neutron spin echo amplitude and phase in forward transmission as a function of the phase current in the spectrometer. Panel (a) is an example of a heat map of the intensity of neutron counts across the range of incident neutron wavelengths used as a function of the phase current for the sample at $T = 230$ K. Panels (b) - (f) show a sum over the range of wavelengths used in the measurement at each value for the phase current at the following temperatures: 230 K (b), 240 K (c), 251 K (d), 260 K (e), and 270 K (f). The spin echo condition in paramagnetic mode occurs at the value of the phase current which minimizes this sum and for which the signal minimum is wavelength-independent, as indicated by the vertical dashed line in the plots.

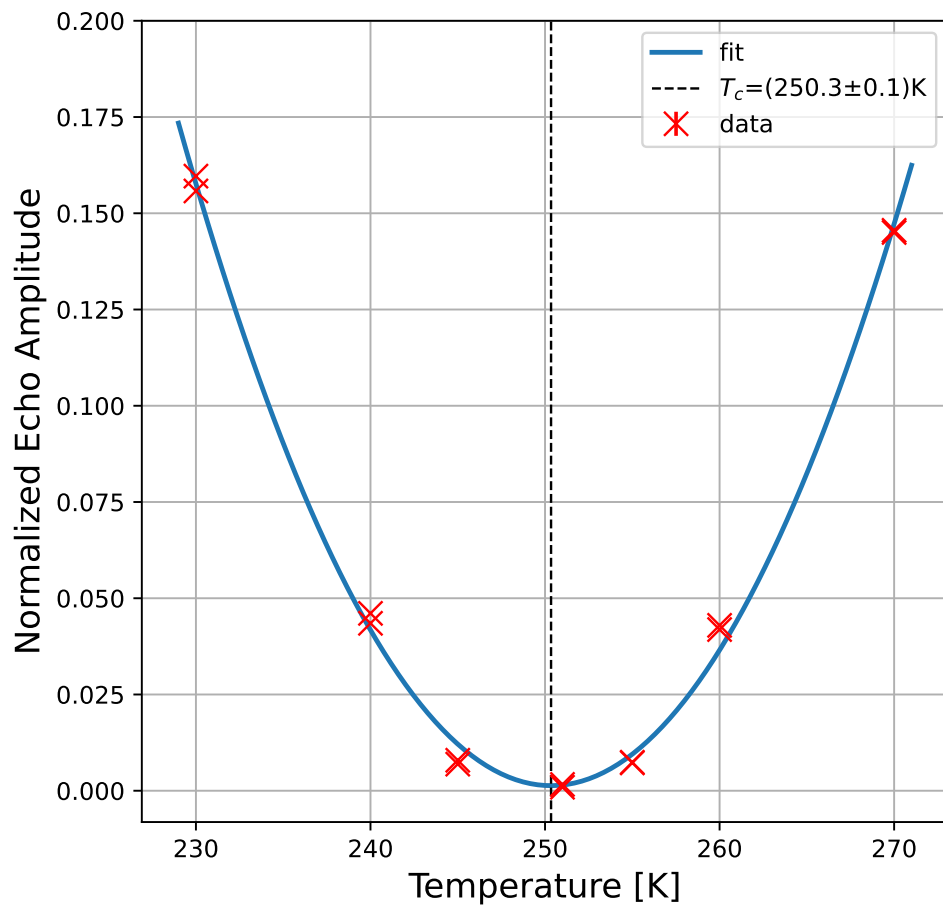


Figure 7: Plot of the centroid amplitude with a minimum around $T = 250.3$ K. The centroid amplitude is proportional to the magnetic moment of the sample with the neutron spin echo spectrometer operated in paramagnetic spin-flipping mode as shown in the data of Fig. 6. The temperature where the spin echo amplitude is consistent with zero within statistical error is also consistent with the temperature T_{comp} as determined by the SQUID external field measurements shown above and with compensation temperature measurements made in-situ.

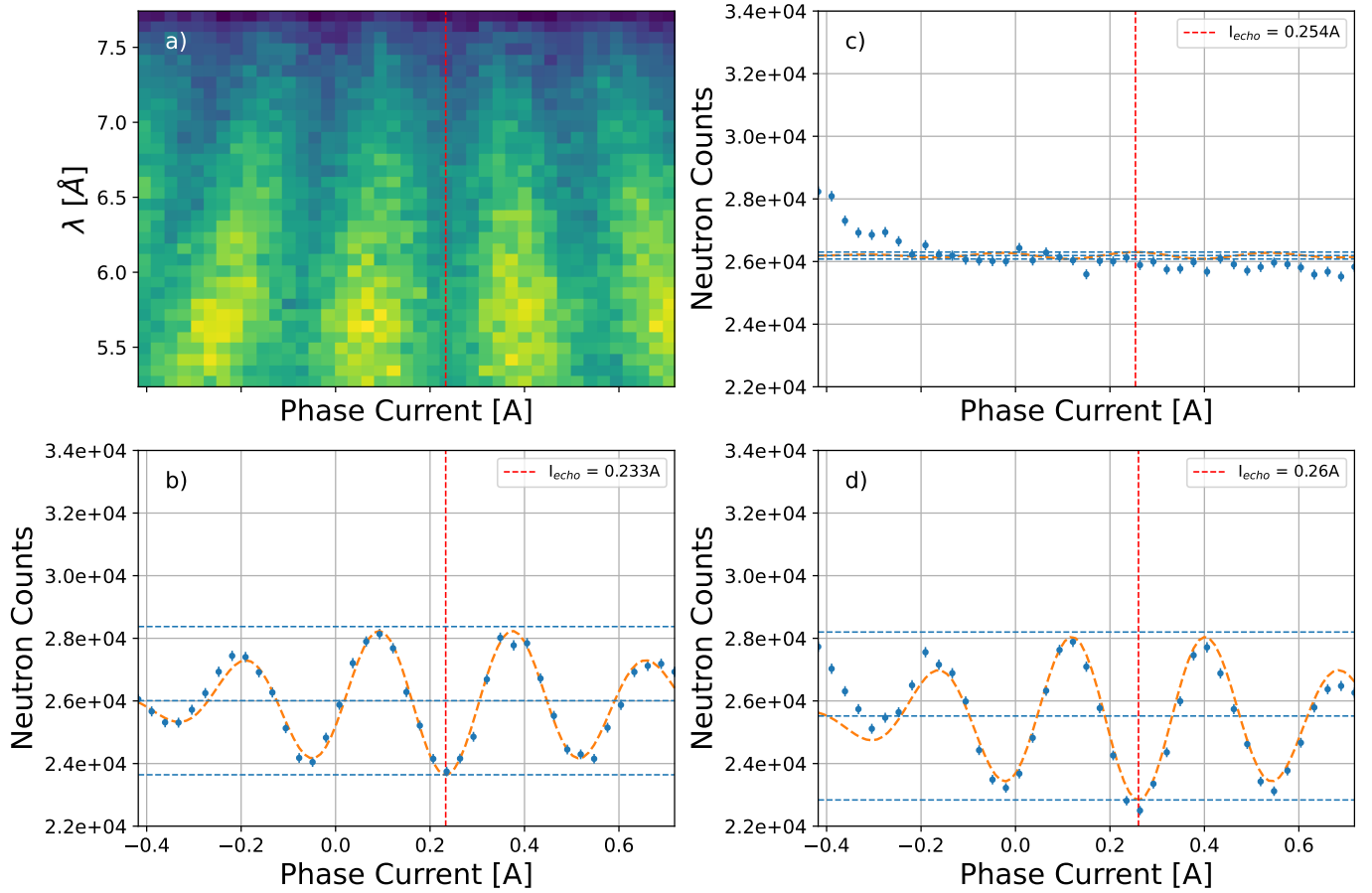


Figure 8: Plots of the neutron spin echo amplitude and phase as a function of the phase current in the spectrometer. In this case, the downstream arm of the spectrometer is set to an angle of 4 deg relative to the incident neutron momentum. Panel (a) is an example of a heat map of the intensity of neutron counts across the range of incident neutron wavelengths used as a function of the phase current for the sample at $T = 240$ K. Panels (b) - (d) show a sum over the range of wavelengths used in the measurement at each value for the phase current at the following temperatures: 240 K (b), 251 K (c), and 260 K (d). The spin echo condition in paramagnetic mode occurs at the value of the phase current which minimizes this sum and for which the signal minimum is wavelength-independent, as indicated by the vertical dashed line in the plots.

These data were taken to check our understanding of the paramagnetic scattering from the sample. In paramagnetic neutron scattering, only the fluctuations in the internal magnetization normal to the momentum transfer direction \vec{Q} cause neutron spin flip scattering and therefore contribute to the neutron spin echo signal. Since the sample was magnetized along the axis of the cylindrical sample which in turn is parallel to the incident neutron momentum and therefore normal to \vec{Q} , we expected to see a paramagnetic spin echo signal away from T_{comp} but nothing at T_{comp} as in the transmission data. The data indeed shows this behavior as expected, thereby confirming again that the internal magnetization in the sample away from T_{comp} points in the expected direction. Furthermore, the agreement between T_{comp} as inferred from the $Q = 0$ and $Q \neq 0$ data is also consistent within measurement precision with the absence of anisotropic components to the antiferromagnetic ordering from sample impurities. These data, however, possess lower statistical accuracy compared to our transmission data and therefore are not as sensitive to deviations away from T_{comp} .

6. Polarized Neutron Imaging Setup

We used the MARS (Multimodal Advanced Radiography Station) neutron imaging instrument at HFIR, which we augmented to conduct polarized neutron spin rotation measurements. A V-cavity polarizer in the slow neutron beam upstream of the target produced a high polarization transverse to the momentum. The neutron spin was adiabatically transported into a mu-metal magnetic shield and into the sample region. A sharp, nonadiabatic neutron spin transition after the sample region was established using a Forte-style V-coil followed by a longitudinal solenoidal magnetic field. This combination of magnetic fields adiabatically transported the component of the neutron spin which rotated about the neutron beam axis upon traversing the sample region and guided it into the neutron beam direction, where it was analyzed using a longitudinally-polarized ^3He neutron spin filter based on spin-exchange optical pumping. By reversing the direction of the current in the Forte coil, this combination of fields reversed the direction of the transported rotated neutron spin component. The spin rotation angle could then be extracted from the asymmetry in the neutron intensity transmitted through the polarization analyzer, according to:

$$PA \sin \phi = \frac{N_+ - N_-}{N_+ + N_-} . \quad (1)$$

Here, N_+ and N_- are the neutron transmission intensities through the polarization analyzer for the two directions in the Forte coil, P is the neutron polarization (≈ 0.95), A is the analyzing power of the neutron polarization analyzer (≈ 0.86), and ϕ is the neutron spin rotation angle. Figure 10a shows a block diagram of the neutron

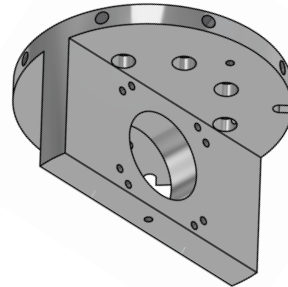


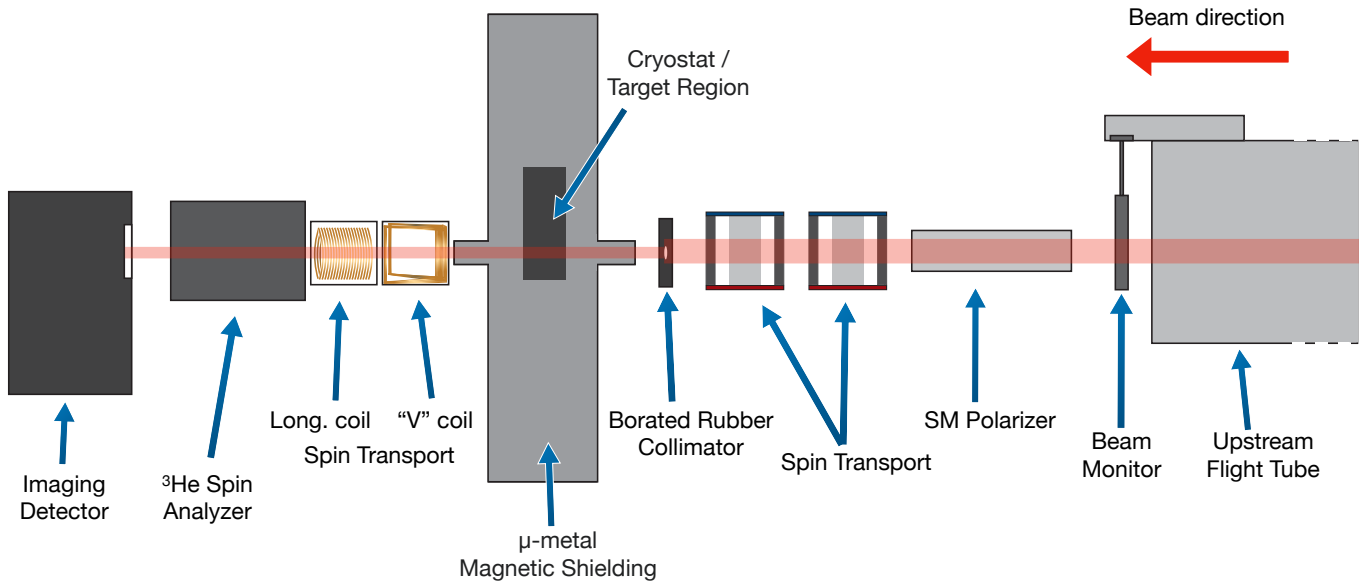
Figure 9: The single-cell sample holder used in the 2023 MARS experiment.

spin transport components and Figure 10b illustrates the spin manipulations occurring at each stage.

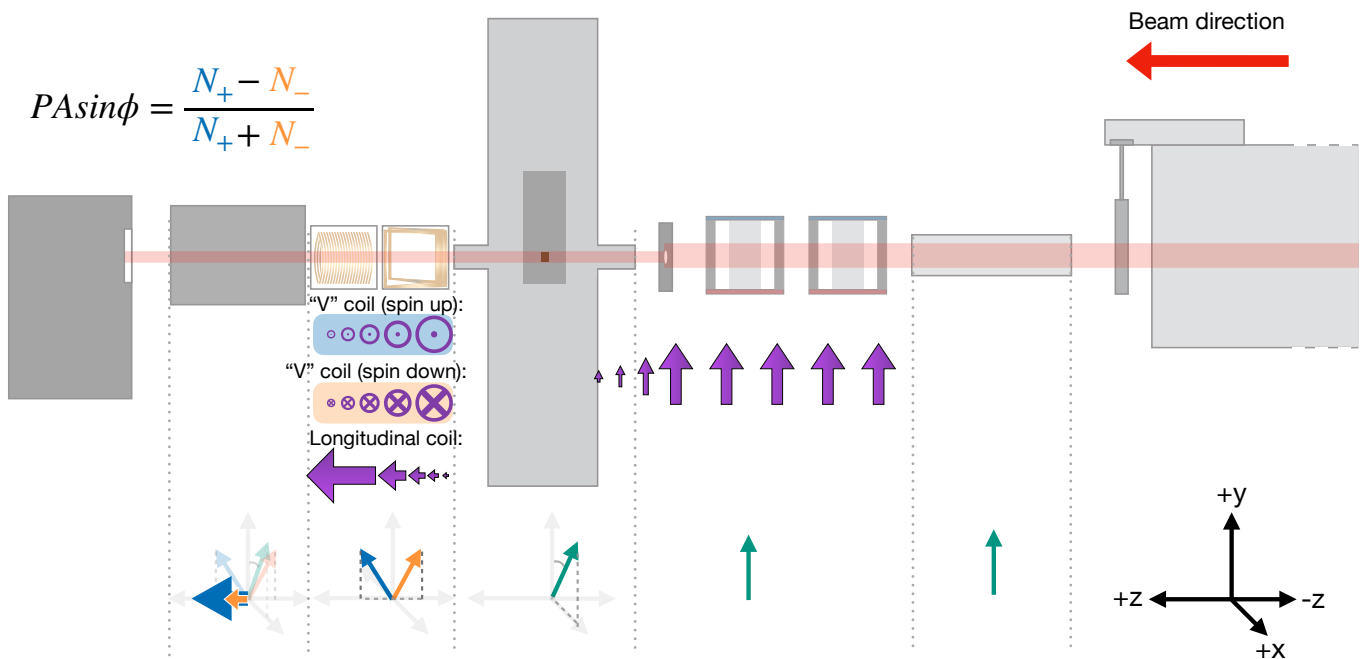
The TbIG sample was mounted with its axis of magnetization along the neutron beam direction (along the z axis in Figure 10b) so that any nonzero sample magnetization along the neutron beam axis would rotate the neutron spin in a direction that would be caught by the neutron polarimeter (in the xy plane as shown in Figure 10b). The neutron polarimeter was calibrated by applying a small longitudinal magnetic field just outside the entrance to the magnetic shield and confirming the expected neutron spin rotation angle from Larmor precession.

Much of the same instrumentation from the SNS-NSE experiment was used to mount and cool the TbIG sample, with slight modifications. The sample holder design is shown in Figure 9. The TbIG sample was contained in a single-cell aluminum sample holder with sapphire windows placed in good thermal contact on both ends of the cylindrical sample and on the sample holder. Silicon diode thermometry determined the sample temperature to 10 mK precision. The cell was surrounded by an aluminum radiation shield and held in the vacuum chamber of a Cryo Industries RC102 cryostat with sapphire optical access windows. The cryostat was cooled using a slow stream of liquid nitrogen whose flow rate was set to bring the target temperature close enough to the temperatures of interest that the fine temperature control could be realized using a PID feedback system with a heater on the sample. Temperature stability of 50 mK was realized as data were collected in a 2.5 K band around T_{comp} in 0.5 K steps. A fluxgate magnetometer just outside the cryostat vacuum near the cell was used to monitor the magnetic field inside the magnetic shield.

The neutron detector was an imaging device with a maximum spatial resolution of ≈ 100 microns [76]. The spatial resolution of this imaging instrument was fine enough, in combination with the choices of neutron beam collimation made for this measurement, to identify macroscopic



(a) Block diagram of the neutron spin transport elements installed on the MARS beamline.



(b) Block diagram of the neutron spin manipulations occurring at each stage along the beamline.

Figure 10: Block diagrams of the neutron spin transport elements installed in the MARS beamline. Each component is labeled in (a). The neutron spin manipulation is shown in (b): purple arrows represent magnetic fields, green arrows represent the direction of neutron spin, and blue and orange arrows represent positive and negative rotations of the neutron spin, respectively.

magnetic domains of size $\approx 1\text{mm} \times 1\text{mm}$ from the neutron spin rotation angle measured at each temperature [12] if they exist. The results of a detailed analysis to search for any evidence of domain structure in our ferrimagnetic sample will be presented in a later paper.

7. Polarized Neutron Spin Rotation Images

Figure 11 shows a sequence of neutron image pairs for the two different settings of the neutron polarimeter at three different temperatures: one pair above T_{comp} , one pair at T_{comp} as inferred from the measurements of the external magnetic field and the neutron spin echo data, and one pair below T_{comp} . The neutron wavelength distribution used was that from the cold neutron source viewed by the MARS instrument as modified downstream by the upstream neutron guide and neutron supermirror polarizer; the mean neutron wavelength was 2.8 \AA . These sequences of images clearly show the internal magnetization inside the ferrimagnet vanishing at T_{comp} and reversing sign on either side of T_{comp} . In addition, Figure 12 shows the measured neutron spin rotation angles at different temperatures. A quadratic fit to the data gives rotation angles of 0.82 and -0.62 radians at 10 K below and above $T_{comp} = 250\text{ K}$, and 0 radians at $T = T_{comp}$, supporting the conclusion that the magnetization of the sample vanished at T_{comp} .

The magnetization results can be compared to a molecular field model of ferrimagnetic garnets, which is described in detail in [45] and is briefly summarized here. A three-sublattice model of TbIG is used with a Tb^{3+} dodecahedral site denoted c , an Fe^{3+} octahedral site denoted a , and an Fe^{3+} tetrahedral site denoted d . As functions of temperature, the total magnetization per molecule of each sublattice is given by the starting magnetization multiplied by Brillouin functions B_J :

$$\begin{aligned} M_c(T) &= M_c(0)B_{J_c}(x_c) \\ M_a(T) &= M_a(0)B_{J_a}(x_a) \\ M_d(T) &= M_d(0)B_{J_d}(x_d). \end{aligned} \quad (2)$$

The Boltzmann energy ratios in eq. 2 are given by:

$$\begin{aligned} x_c &= \frac{g_c J_c \mu_B}{k_B T} [N_{cc}M_c + N_{ac}M_a + N_{dc}M_d] \\ x_a &= \frac{g_a J_a \mu_B}{k_B T} [N_{ac}M_c + N_{aa}M_a + N_{ad}M_d] \\ x_d &= \frac{g_d J_d \mu_B}{k_B T} [N_{cd}M_c + N_{ad}M_a + N_{dd}M_d], \end{aligned} \quad (3)$$

where the N_{ij} are the molecular field coefficients. The coefficients (in mol/cm^3) are $N_{ac} = -4.2$, $N_{dc} = 6.5$, $N_{cc} = 0$, $N_{aa} = -65$, $N_{ad} = 97$, and $N_{dd} = -30.4$, taken from previous work [15, 28].

The molecular field model, corrected for small admixtures of orthoferrite and hematite (with moments described

in [71, 3]), predicts magnetization values of 2589 A/m and -2328 A/m , at 10 K below and above T_{comp} , for the TbIG sample used in the NSE and imaging experiments. The predicted neutron spin rotation angles, based on the integration of the analytical expression of the longitudinal field on the axis of the sample with the above magnetizations, are 2.79 radians and -2.50 radians at these temperatures.

We note that the N_{ij} in the model result from fits to the spontaneous moments obtained from high-field data extrapolated to zero applied field from the linear parts of garnet hysteresis curves, and represent the fully saturated moments. The actual remanent magnetization we observe in our powder TbIG samples is smaller by a factor that varies somewhat with temperature. Fig. 13 shows a hysteresis curve for a powder TbIG sample at 260 K (10 K above T_{comp}), measured in a SQUID magnetometer. From the figure, the remanence is approximately 70% of the extrapolated moment, which holds for 10 K below T_{comp} as well. This 70% correction appears to hold for our samples arbitrarily close to T_{comp} (at room temperature the factor is closer to 50%), and is sufficient to explain the discrepancy between the model and the SQUID remanence data.

In addition, the sample had not been polarized for at least 6 months prior to the imaging measurements at MARS (activation in the NSE beam precluded handling of the sample). At polarization, just before the NSE measurements, the surface field was measured to be 16.3 Gauss. Immediately prior to the MARS imaging run, we did manage a rudimentary measurement of the sample surface field with a hand-held Gaussmeter, which registered 5 Gauss approximately 2 mm above the surface. This suggests a demagnetization factor of about $1/3$, which would affect all measurements correlated with the magnetization, including the spin rotation.

Applying the appropriate remanent scaling and demagnetization factors to the model predictions for the neutron imaging sample yields magnetizations of 617 A/m and -555 A/m , and associated neutron spin rotation angles of 0.67 ± 0.12 radians and -0.60 ± 0.11 radians, at 10 K below and above T_{comp} . Here, we have included error from the remanence correction (the extrapolation in Fig. 13), the surface field measurement (0.5 mm position error in the Gaussmeter probe), sample temperature (2 K), and we allow for 1% variation in the N_{ij} .

An important prediction from the model is the (excess) electron spin density at T_{comp} . Using the N_{ij} above and applying the 70% correction factor yields a value of $-0.37 \pm 0.02\text{ uB/molecule}$. This prediction is also reduced by the sample purity, and depolarization factor affecting the spin rotation in the imaging measurements. The spin excess adjusted for these effects is $-0.11 \pm 0.02\text{ uB/molecule}$.

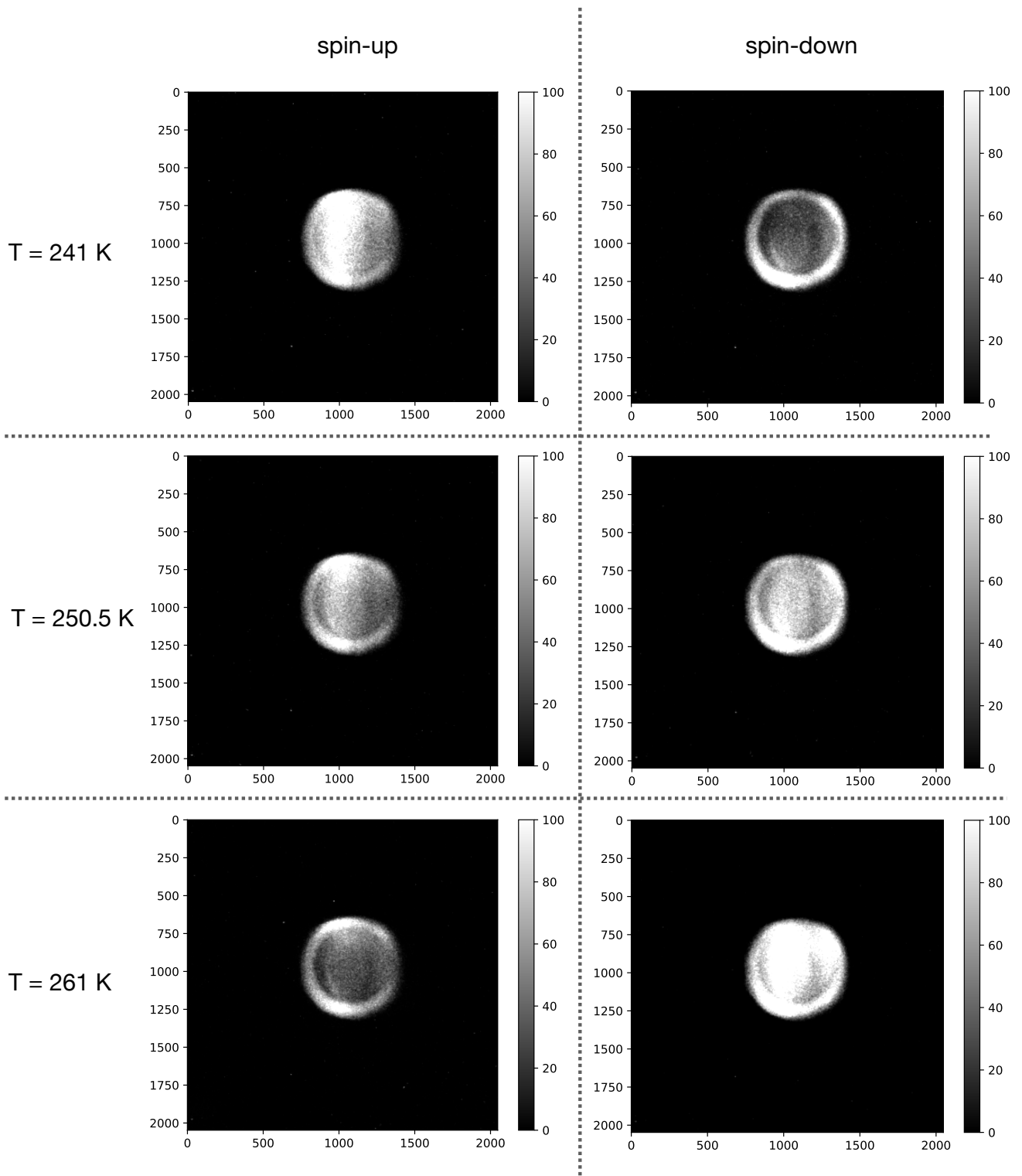


Figure 11: Radiographs of TbIG under different spin orientations and temperatures. The exposure time of each radiograph is 300 seconds with a $300\ \mu\text{m}$ -thick RC Tritec ${}^6\text{LiF/ZNS:Cu}$ (ratio 1/2) scintillator. The axes for each image refer to pixel number for a 2048×2048 pixel CCD camera detector. The same pixel intensity grayscale bar is used for all images. For a given spin state of neutrons in the beam (spin-up in the left column and spin-down in the right column of the plots), we see a transition from low to high (or high to low) intensity above and below the compensation temperature T_{comp} . Very close to T_{comp} , we see similar intensities implying roughly equal transmission for each spin state.

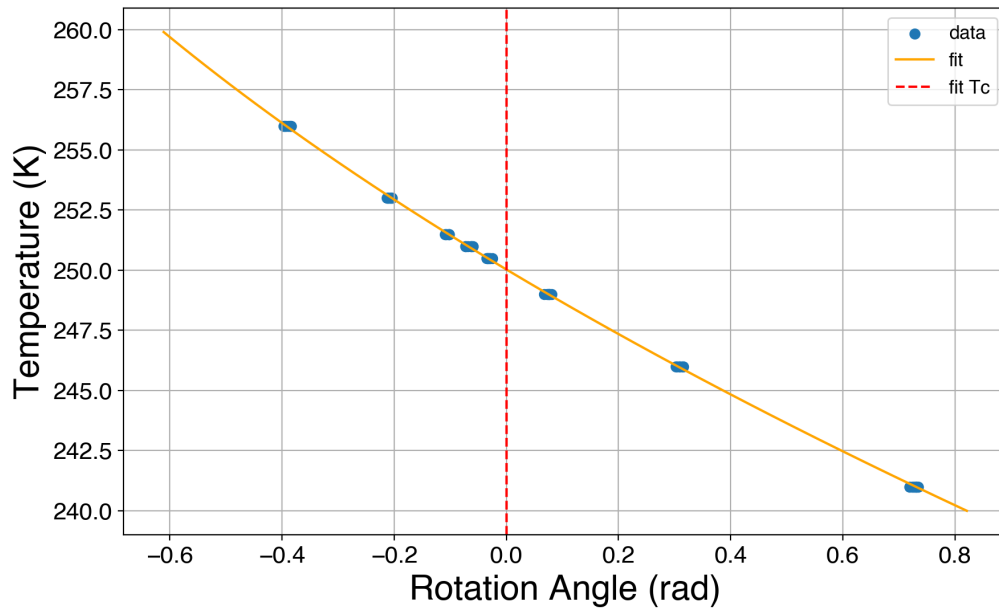


Figure 12: Plot of neutron spin rotation vs temperature and quadratic fit with x-intercept of $T_{comp} = 250.03 \pm 0.03$ K.

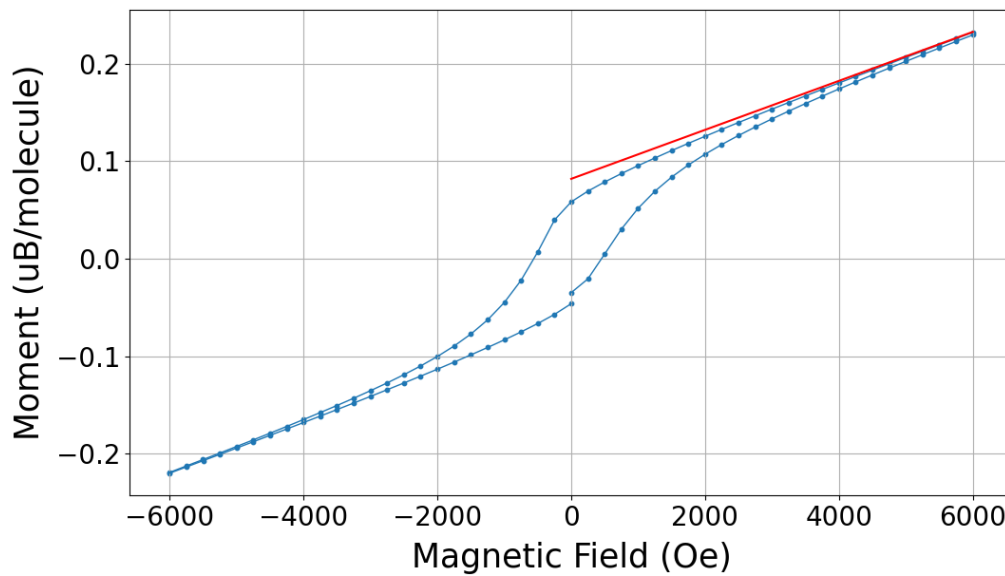


Figure 13: Moment vs. magnetic field hysteresis plot for a powder sample of TbIG at 260 K. From this curve we see that at $T_{comp} + 10$ K, the remnant magnetization is $0.058 \mu_B/\text{mol}$, and the value extrapolated back from the linear behavior at high fields is $0.08 \mu_B/\text{mol}$.

8. Conclusions and Future Work

We conclude from the evidence of all of the measurements described above that the internal magnetization of the ferrimagnet TbIG at and near its compensation temperature T_{comp} over macroscopic internal distance scales larger than 1 mm behaves according to the usual macroscopic models of ferrimagnetism and possesses a vanishing magnetization at T_{comp} .

We are conducting a more detailed analysis of the neutron spin rotation 2D image data to attempt to quantify the properties of any possible microscale ferrimagnetic domains that might be present in this material. This type of investigation is accessible through polarized neutron imaging but not to any external probe of the magnetization.

With the same sample used in this work, we also conducted measurements at T_{comp} in which we repeatedly rotated the sample 180 degrees about a vertical axis, thereby reversing the direction of the nonzero net electron spin polarization in the material, which was set by the prior sample magnetization to point along the cylinder axis and therefore along the neutron beam momentum. If a spin-dependent exotic interaction exists proportional to $\vec{s}_n \cdot \vec{s}_e$ where \vec{s}_n is the neutron spin and \vec{s}_e is the electron spin, then the transversely-polarized neutron spin would rotate about the neutron beam axis with an angle that reverses in sign upon reversal of \vec{s}_e . We will report the results of this analysis in a later work.

Acknowledgements

The authors would like to acknowledge the contributions of Maren Pink at IU's Molecular Structure Center for her help with the x-ray diffractometry. The diffractometry was primarily conducted on a Bruker Venture D8 diffractometer. Support for the acquisition of the Bruker Venture D8 diffractometer through the Major Scientific Research Equipment Fund from the President of Indiana University and the Office of the Vice President for Research is gratefully acknowledged. Additional diffractometry was conducted on a PANalytical Empyrean multipurpose diffractometer, which is supported by National Science Foundation grant number NSF/CHE-1048613. K. N. Lopez, M. Luxnat, M. Van Meter, S. Samiei, and W. M. Snow acknowledge support from US National Science Foundation (NSF) grants PHY-1913789 and PHY-2209481 and the Indiana University Center for Spacetime Symmetries. K. N. Lopez also acknowledges the support of the National GEM Consortium and the Indiana Space Grant Consortium. M. Sarsour and T. Mulkey acknowledge support from US Department of Energy grant DE-SC0010443. J. C. Long and B. Hill acknowledge support from US National Science Foundation (NSF) grant PHY-1707986. The authors acknowledge the use of facilities and instrumentation supported by NSF through the University of Illinois Materials Research Science and Engineering Center DMR-2309037. This research used resources at the High Flux Isotope Reactor and the Spallation Neutron Source, both DOE Office of Science User Facilities operated by the Oak Ridge Na-

tional Laboratory.

References

- [1] E. G. Adelberger, J. H. Gundlach, B. R. Heckel, S. Hoedl, and S. Schlamminger. Torsion balance experiments: A low-energy frontier of particle physics. *Prog. Part. Nucl. Phys.*, 62:102–134, 2009. doi: 10.1016/j.pnpnp.2008.08.002. 2
- [2] S. Afach, G. Ban, G. Bison, K. Bodek, M. Burghoff, M. Daum, M. Fertl, B. Franke, Z. D. Grujić, V. H elaine, M. Kasprzak, Y. Kermaidic, K. Kirch, P. Knowles, H.-C. Koch, S. Komposch, A. Kozela, J. Krempel, B. Lauss, T. Lefort, Y. Lemi ere, A. Mtchedlishvili, O. Naviliat-Cuncic, F. M. Piegsa, G. Pignol, P. N. Prashanth, G. Qu em ener, D. Rebreyend, D. Ries, S. Rocca, P. Schmidt-Wellenburg, A. Schnabel, N. Severijns, J. Voigt, A. Weis, G. Wyszynski, J. Zejma, J. Zenner, and G. Zsigmond. Constraining interactions mediated by axion-like particles with ultracold neutrons. *Physics Letters B*, 745:58–63, 2015. ISSN 0370-2693. doi: <https://doi.org/10.1016/j.physletb.2015.04.024>. URL <https://www.sciencedirect.com/science/article/pii/S0370269315002671>. 2
- [3] J. Andr e-Filho, L. Le on-F elix, J. Coaquira, V. Garg, and A. de Oliveira. Size dependence of the magnetic and hyperfine properties of nanostructured hematite (α -Fe₂O₃) powders prepared by the ball milling technique. *Hyperfine Interact.*, page 224, 2014. URL <https://doi.org/10.1007/s10751-013-0850-5>. 3, 11
- [4] R. Azis, M. Mustaffa, N. md. shahrani, N. Abdullah, R. Nazlan, F. Mohd Idris, I. Ismail, M. Zulkimi, I. R. Ibrahim, Z. Abbas, and N. mohd saiden. Influence of sintering temperature on the structural, electrical and microwave properties of yttrium iron garnet (yig). *Journal of Materials Science: Materials in Electronics*, 29, 05 2018. doi: 10.1007/s10854-018-8850-5. 3
- [5] N. G. Baazov and A. G. Mandzhavidze. A study of rare-earth magnetics by neutron methods. *NASA STI/Recon Technical Report A*, 84:21567, Jan. 1983. 4
- [6] S. B aebler, V. V. Nesvizhevsky, K. V. Protasov, and A. Y. Voronin. Constraint on the coupling of axionlike particles to matter via an ultracold neutron gravitational experiment. *Phys. Rev. D*, 75:075006, Apr 2007. doi: 10.1103/PhysRevD.75.075006. URL <https://link.aps.org/doi/10.1103/PhysRevD.75.075006>. 2
- [7] J. J. Bara, A. T. Pedziwiatr, W. Zarek, Z. Kucharski, and J. Suwalski. Investigations of crystal and magnetic properties of the Dy₆Fe₂₃ intermetallic compound. *Journal of the Less Common Metals*, 84:93–98, 1982. ISSN 0022-5088. doi: [https://doi.org/10.1016/0022-5088\(82\)90132-1](https://doi.org/10.1016/0022-5088(82)90132-1). URL <https://www.sciencedirect.com/science/article/pii/0022508882901321>. 1
- [8] M. Bonnet, A. Delapalme, H. Fuess, and P. Becker. Polarized neutron study of covalency effects in yttrium iron garnet. *Journal of Physics and Chemistry of Solids*, 40(11):863–876, 1979. ISSN 0022-3697. doi: [https://doi.org/10.1016/0022-3697\(79\)90042-8](https://doi.org/10.1016/0022-3697(79)90042-8). URL <https://www.sciencedirect.com/science/article/pii/0022369779900428>. 2, 4
- [9] S. M. Carroll and G. B. Field. Consequences of propagating torsion in connection-dynamic theories of gravity. *Phys. Rev. D*, 50:3867–3873, Sep 1994. doi: 10.1103/PhysRevD.50.3867. URL <https://link.aps.org/doi/10.1103/PhysRevD.50.3867>. 2
- [10] T. Chatterji, editor. *Neutron scattering from magnetic materials*. Elsevier, Amsterdam ; Boston, 1st ed edition, 2006. ISBN 978-0-444-51050-1. OCLC: ocm61748467. 5
- [11] G. Cronenberg, P. Brax, H. Filter, P. Geltenbort, T. Jenke, G. Pignol, M. Pitschmann, M. Thalhammer, and H. Abele. Acoustic Rabi oscillations between gravitational quantum states and impact on symmetron dark energy. *Nature Physics*, 14(10):1022–1026, Oct. 2018. ISSN 1745-2481. doi: 10.1038/s41567-018-0205-x. URL <https://doi.org/10.1038/s41567-018-0205-x>. 2
- [12] I. Dhiman, R. Ziesche, T. Wang, H. Bilheux, L. Santodonato, X. Tong, C. Jiang, I. Manke, W. Treimer, T. Chatterji, and

- N. Kardjilov. Setup for polarized neutron imaging using in situ 3 he cells at the oak ridge national laboratory high flux isotope reactor cg-1d beamline. *Review of Scientific Instruments*, 88: 095103, 09 2017. doi: 10.1063/1.5001525. 11
- [13] G. F. Dionne. Molecular Field and Exchange Constants of Gd³⁺-Substituted Ferrimagnetic Garnets. *Journal of Applied Physics*, 42(5):2142–2143, Apr. 1971. ISSN 0021-8979, 1089-7550. doi: 10.1063/1.1660506. URL <https://pubs.aip.org/jap/article/42/5/2142/168729/Molecular-Field-and-Exchange-Constants-of-Gd3>. 1
- [14] G. F. Dionne. Molecular-field coefficients of rare-earth iron garnets. *Journal of Applied Physics*, 47(9):4220–4221, Sept. 1976. ISSN 0021-8979, 1089-7550. doi: 10.1063/1.323204. URL <https://pubs.aip.org/jap/article/47/9/4220/502208/Molecular-field-coefficients-of-rare-earth-iron>. 1
- [15] G. F. Dionne. *Magnetic Oxides*. Springer US, Boston, MA, 2009. ISBN 978-1-4419-0053-1 978-1-4419-0054-8. doi: 10.1007/978-1-4419-0054-8. URL <http://link.springer.com/10.1007/978-1-4419-0054-8>. 1, 11
- [16] B. A. Dobrescu and I. Mocioiu. Spin-dependent macroscopic forces from new particle exchange. *JHEP*, 11:005, 2006. doi: 10.1088/1126-6708/2006/11/005. 2
- [17] D. Dubbers and M. G. Schmidt. The neutron and its role in cosmology and particle physics. *Rev. Mod. Phys.*, 83:1111–1171, Oct 2011. doi: 10.1103/RevModPhys.83.1111. URL <https://link.aps.org/doi/10.1103/RevModPhys.83.1111>. 2
- [18] P. Fadeev, Y. V. Stadnik, F. Ficek, M. G. Kozlov, V. V. Flambaum, and D. Budker. Revisiting spin-dependent forces mediated by new bosons: Potentials in the coordinate-space representation for macroscopic- and atomic-scale experiments. *Phys. Rev. A*, 99:022113, Feb 2019. doi: 10.1103/PhysRevA.99.022113. URL <https://link.aps.org/doi/10.1103/PhysRevA.99.022113>. 2
- [19] V. Flambaum and Y. Stadnik. Searches for New Particles Including Dark Matter with Atomic, Molecular and Optical Systems. In G. W. F. Drake, editor, *Springer Handbook of Atomic, Molecular, and Optical Physics*, pages 461–469. Springer International Publishing, Cham, 2023. ISBN 978-3-030-73893-8. doi: 10.1007/978-3-030-73893-8_31. URL https://doi.org/10.1007/978-3-030-73893-8_31. 2
- [20] A. Frank, P. V. Isacker, and J. Gómez-Camacho. Probing additional dimensions in the universe with neutron experiments. *Physics Letters B*, 582(1):15–20, 2004. ISSN 0370-2693. doi: <https://doi.org/10.1016/j.physletb.2003.12.026>. URL <https://www.sciencedirect.com/science/article/pii/S0370269303019282>. 2
- [21] H. Fuess, G. Bassi, M. Bonnet, and A. Delapalme. Neutron scattering length of terbium structure refinement and magnetic moments of terbium iron garnet. *Solid State Communications*, 18(5):557–562, 1976. ISSN 0038-1098. doi: [https://doi.org/10.1016/0038-1098\(76\)91480-0](https://doi.org/10.1016/0038-1098(76)91480-0). URL <https://www.sciencedirect.com/science/article/pii/0038109876914800>. 4
- [22] H. Fuess, M. Bonnet, and A. Delapalme. Determining the magnetic moments, form factors and the spin density in yttrium-(YIG) and terbium-iron-granate (TbIb) with polarized neutrons. Technical report, Germany, 1976. AED-Conf-76-033-005 INIS Reference Number: 7271613. 4
- [23] S. Geller, J. P. Remeika, R. C. Sherwood, H. J. Williams, and G. P. Espinosa. Magnetic study of the heavier rare-earth iron garnets. *Phys. Rev.*, 137:A1034–A1038, Feb 1965. doi: 10.1103/PhysRev.137.A1034. URL <https://link.aps.org/doi/10.1103/PhysRev.137.A1034>. 1
- [24] M. J. Geselbracht, A. M. Cappellari, A. B. Ellis, M. A. Rzeznik, and B. J. Johnson. Rare Earth Iron Garnets: Their Synthesis and Magnetic Properties. *Journal of Chemical Education*, 71(8):696, Aug. 1994. ISSN 0021-9584. doi: 10.1021/ed071p696. 1. URL <https://doi.org/10.1021/ed071p696.1>. Publisher: American Chemical Society. 3
- [25] C. Haddock, J. Amadio, E. Anderson, L. Barrón-Palos, B. Crawford, C. Crawford, D. Esposito, W. Fox, I. Francis, J. Fry, H. Gardiner, A. Holley, K. Korsak, J. Lieffers, S. Magers, M. Maldonado-Velázquez, D. Mayorov, J. S. Nico, T. Okudaira, C. Paudel, S. Santra, M. Sarsour, H. M. Shimizu, W. M. Snow, A. Sprow, K. Steffen, H. E. Swanson, F. Toveson, J. Vanderwerp, and P. A. Yergeau. A search for possible long range spin dependent interactions of the neutron from exotic vector boson exchange. *Physics Letters B*, 783:227–233, 2018. ISSN 0370-2693. doi: <https://doi.org/10.1016/j.physletb.2018.06.066>. URL <https://www.sciencedirect.com/science/article/pii/S0370269318305227>. 2
- [26] C. C. Haddock, N. Oi, K. Hirota, T. Ino, M. Kitaguchi, S. Matsumoto, K. Mishima, T. Shima, H. M. Shimizu, W. M. Snow, and T. Yoshioka. Search for deviations from the inverse square law of gravity at nm range using a pulsed neutron beam. *Phys. Rev. D*, 97:062002, Mar 2018. doi: 10.1103/PhysRevD.97.062002. URL <https://link.aps.org/doi/10.1103/PhysRevD.97.062002>. 2
- [27] R. T. Hammond. Torsion gravity. *Reports on Progress in Physics*, 65(5):599, mar 2002. doi: 10.1088/0034-4885/65/5/201. URL <https://dx.doi.org/10.1088/0034-4885/65/5/201>. 2
- [28] P. Hansen, K. Enke, and G. Winkler. 1.2.2.1.2 molecular field- and exchange constants: Datasheet from landolt-börnstein - group iii condensed matter · volume 12a: “part a: Garnets and perovskites” in springer-materials (<https://doi.org/10.1007/10201632.20>). URL https://materials.springer.com/lb/docs/sm_lbs_978-3-540-37375-9_20. Copyright 1978 Springer-Verlag Berlin Heidelberg. 11
- [29] B. Heacock, T. Fujiie, R. W. Haun, A. Henins, K. Hirota, T. Hosobata, M. G. Huber, M. Kitaguchi, D. A. Pushin, H. Shimizu, M. Takeda, R. Valdillez, Y. Yamagata, and A. R. Young. Pendellösung interferometry probes the neutron charge radius, lattice dynamics, and fifth forces. *Science*, 373(6560): 1239–1243, 2021. doi: 10.1126/science.abc2794. URL <https://www.science.org/doi/abs/10.1126/science.abc2794>. 2
- [30] F. W. Hehl, P. von der Heyde, G. D. Kerlick, and J. M. Nester. General relativity with spin and torsion: Foundations and prospects. *Rev. Mod. Phys.*, 48:393–416, Jul 1976. doi: 10.1103/RevModPhys.48.393. URL <https://link.aps.org/doi/10.1103/RevModPhys.48.393>. 2
- [31] J. F. Herbst and J. J. Croat. Magnetization of RFe₃ intermetallic compounds: Molecular field theory analysis. *Journal of Applied Physics*, 53(6):4304–4308, June 1982. ISSN 0021-8979. doi: 10.1063/1.331207. URL <https://doi.org/10.1063/1.331207>. 1
- [32] J. F. Herbst and J. J. Croat. Magnetization of R₆Fe₂₃ intermetallic compounds: Molecular field theory analysis. *Journal of Applied Physics*, 55(8):3023–3027, Apr. 1984. ISSN 0021-8979, 1089-7550. doi: 10.1063/1.333293. URL <https://pubs.aip.org/jap/article/55/8/3023/170635/Magnetization-of-R6Fe23-intermetallic-compounds>. 1
- [33] Y. Hirata, D.-H. Kim, S. K. Kim, D.-K. Lee, S.-H. Oh, D.-Y. Kim, T. Nishimura, T. Okuno, Y. Futakawa, H. Yoshikawa, A. Tsukamoto, Y. Tserkovnyak, Y. Shiota, T. Moriyama, S.-B. Choe, K.-J. Lee, and T. Ono. Vanishing skyrmion Hall effect at the angular momentum compensation temperature of a ferrimagnet. *Nature Nanotechnology*, 14(3):232–236, Jan. 2019. doi: 10.1038/s41565-018-0345-2. 1
- [34] J. Jaeckel and A. Ringwald. The low-energy frontier of particle physics. *Annual Review of Nuclear and Particle Science*, 60:405–437, 2010. URL <https://api.semanticscholar.org/CorpusID:53125975>. 2
- [35] T. Jenke, G. Cronenberg, J. Burgdörfer, L. A. Chizhova, P. Geltenbort, A. N. Ivanov, T. Lauer, T. Lins, S. Rotter, H. Saul, U. Schmidt, and H. Abele. Gravity resonance spectroscopy constrains dark energy and dark matter scenarios. *Phys. Rev. Lett.*, 112:151105, Apr 2014. doi: 10.1103/PhysRevLett.112.151105. URL <https://link.aps.org/doi/10.1103/PhysRevLett.112.151105>. 2
- [36] Y. Kamiya, K. Itagaki, M. Tani, G. N. Kim, and S. Komamiya. Constraints on new gravitylike forces in the nanome-

- ter range. *Phys. Rev. Lett.*, 114:161101, Apr 2015. doi: 10.1103/PhysRevLett.114.161101. URL <https://link.aps.org/doi/10.1103/PhysRevLett.114.161101>. 2
- [37] T. Keller, H. Trepka, K. Habicht, and B. Keimer. Neutron Spin-Echo Instrumentation for Magnetic Scattering. *physica status solidi (b)*, 259(5):2100164, 2022. ISSN 1521-3951. doi: 10.1002/pssb.202100164. URL <https://www.onlinelibrary.wiley.com/doi/abs/10.1002/pssb.202100164>. 5
- [38] C. P. Khattak and F. F. Wang. Perovskites and garnets. Technical Report BNL-21638, Brookhaven National Lab. (BNL), Upton, NY (United States), Upton, NY (United States), Jan. 1976. 3
- [39] K.-J. Kim, S. K. Kim, Y. Hirata, S.-H. Oh, T. Tono, D.-H. Kim, T. Okuno, W. S. Ham, S. Kim, G. Go, Y. Tserkovnyak, A. Tsukamoto, T. Moriyama, K.-J. Lee, and T. Ono. Fast domain wall motion in the vicinity of the angular momentum compensation temperature of ferrimagnets. *Nature Materials*, 16(12):1187–1192, Dec 2017. ISSN 1476-4660. doi: 10.1038/nmat4990. URL <https://doi.org/10.1038/nmat4990>. 1
- [40] H. Leeb and J. Schmiedmayer. Constraint on hypothetical light interacting bosons from low-energy neutron experiments. *Phys. Rev. Lett.*, 68:1472–1475, Mar 1992. doi: 10.1103/PhysRevLett.68.1472. URL <https://link.aps.org/doi/10.1103/PhysRevLett.68.1472>. 2
- [41] R. Lehnert, W. M. Snow, and H. Yan. A first experimental limit on in-matter torsion from neutron spin rotation in liquid 4He. *Physics Letters B*, 730:353–356, 2014. ISSN 0370-2693. doi: <https://doi.org/10.1016/j.physletb.2014.01.063>. URL <https://www.sciencedirect.com/science/article/pii/S0370269314000859>. 2
- [42] R. Lehnert, W. M. Snow, Z. Xiao, and R. Xu. Constraining spacetime nonmetricity with neutron spin rotation in liquid 4He. *Physics Letters B*, 772:865–869, 2017. ISSN 0370-2693. doi: <https://doi.org/10.1016/j.physletb.2017.07.059>. URL <https://www.sciencedirect.com/science/article/pii/S0370269317306159>. 2
- [43] J. Leitner and S. Okubo. Parity, charge conjugation, and time reversal in the gravitational interaction. *Phys. Rev.*, 136:B1542–B1546, Dec 1964. doi: 10.1103/PhysRev.136.B1542. URL <https://link.aps.org/doi/10.1103/PhysRev.136.B1542>. 2
- [44] H. Lemmel, P. Brax, A. N. Ivanov, T. Jenke, G. Pignol, M. Pitschmann, T. Potocar, M. Wellenzohn, M. Zawisky, and H. Abele. Neutron interferometry constrains dark energy chameleon fields. *Physics Letters B*, 743:310–314, 2015. ISSN 0370-2693. doi: <https://doi.org/10.1016/j.physletb.2015.02.063>. URL <https://www.sciencedirect.com/science/article/pii/S0370269315001549>. 2
- [45] T. M. Leslie, E. Weisman, R. Khatiwada, and J. C. Long. Prospects for electron spin-dependent short-range force experiments with rare earth iron garnet test masses. *Phys. Rev. D*, 89:114022, Jun 2014. doi: 10.1103/PhysRevD.89.114022. URL <https://link.aps.org/doi/10.1103/PhysRevD.89.114022>. 2, 11
- [46] K. Li, M. Arif, D. G. Cory, R. Haun, B. Heacock, M. G. Huber, J. Nsofini, D. A. Pushin, P. Saggiu, D. Sarenac, C. B. Shahi, V. Skavysh, W. M. Snow, and A. R. Young. Neutron limit on the strongly-coupled chameleon field. *Phys. Rev. D*, 93:062001, Mar 2016. doi: 10.1103/PhysRevD.93.062001. URL <https://link.aps.org/doi/10.1103/PhysRevD.93.062001>. 2
- [47] D. Louca, K. Kamazawa, and T. Proffen. Formation of local electric dipoles with no unique polar axis in $\text{tb}_3\text{fe}_5\text{o}_{12}$. *Phys. Rev. B*, 80:214406, Dec 2009. doi: 10.1103/PhysRevB.80.214406. URL <https://link.aps.org/doi/10.1103/PhysRevB.80.214406>. 2
- [48] H. Man, Z. Shi, G. Xu, Y. Xu, X. Chen, S. Sullivan, J. Zhou, K. Xia, J. Shi, and P. Dai. Direct observation of magnon-phonon coupling in yttrium iron garnet. *Phys. Rev. B*, 96:100406, Sep 2017. doi: 10.1103/PhysRevB.96.100406. URL <https://link.aps.org/doi/10.1103/PhysRevB.96.100406>. 4
- [49] A. G. Mandzhavidze, N. G. Baazov, and E. A. Biryukova. Resonance neutron depolarization of periodical domain structures in terbium-yttrium ferrite-garnet. *Fizika Tverdogo Tela*, 27:2371–2374, Feb. 1985. URL https://www.mathnet.ru/php/archive.phtml?wshow=paper&jrnid=ftt&paperid=2191&option_lang=eng. 4
- [50] F. Mezei. The principles of neutron spin echo. In F. Mezei, editor, *Neutron Spin Echo*, pages 1–26, Berlin, Heidelberg, 1980. Springer. ISBN 978-3-540-39354-2. doi: 10.1007/3-540-10004-0-16. 5
- [51] F. Mezei. Fundamentals of Neutron Spin Echo Spectroscopy. In F. Mezei, C. Pappas, and T. Gutberlet, editors, *Neutron Spin Echo Spectroscopy: Basics, Trends and Applications*, pages 5–14. Springer, Berlin, Heidelberg, 2003. ISBN 978-3-540-45823-4. doi: 10.1007/3-540-45823-9-2. URL <https://doi.org/10.1007/3-540-45823-9-2>. 5
- [52] J. E. Moody and F. Wilczek. New macroscopic forces? *Phys. Rev. D*, 30:130–138, Jul 1984. doi: 10.1103/PhysRevD.30.130. URL <https://link.aps.org/doi/10.1103/PhysRevD.30.130>. 2
- [53] J. Murata and S. Tanaka. A review of short-range gravity experiments in the lhc era. *Classical and Quantum Gravity*, 32(3):033001, Jan 2015. doi: 10.1088/0264-9381/32/3/033001. URL <https://dx.doi.org/10.1088/0264-9381/32/3/033001>. 2
- [54] Y. Nambu, J. Barker, Y. Okino, T. Kikkawa, Y. Shiomi, M. Enderle, T. Weber, B. Winn, M. Graves-Brook, J. M. Tranquada, T. Ziman, M. Fujita, G. E. W. Bauer, E. Saitoh, and K. Kakurai. Observation of magnon polarization. *Phys. Rev. Lett.*, 125:027201, Jul 2020. doi: 10.1103/PhysRevLett.125.027201. URL <https://link.aps.org/doi/10.1103/PhysRevLett.125.027201>. 2, 4
- [55] V. V. Nesvizhevsky, G. Pignol, and K. V. Protasov. Neutron scattering and extra-short-range interactions. *Phys. Rev. D*, 77:034020, Feb 2008. doi: 10.1103/PhysRevD.77.034020. URL <https://link.aps.org/doi/10.1103/PhysRevD.77.034020>. 2
- [56] J. S. Nico and W. M. Snow. Fundamental neutron physics. *Annual Review of Nuclear and Particle Science*, 55(1):27–69, 2005. doi: 10.1146/annurev.nucl.55.090704.151611. URL <https://doi.org/10.1146/annurev.nucl.55.090704.151611>. 2
- [57] Néel, M. Louis. Propriétés magnétiques des ferrites ; ferromagnétisme et antiferromagnétisme. *Ann. Phys.*, 12(3):137–198, 1948. doi: 10.1051/anphys/194812030137. URL <https://doi.org/10.1051/anphys/194812030137>. 1
- [58] C. Pappas, E. Lelièvre-Berna, P. Bentley, E. Bourgeat-Lami, E. Moskvina, M. Thomas, S. Grigoriev, and V. Dyadkin. Polarimetric neutron spin echo: Feasibility and first results. *Nuclear Instruments and Methods in Physics Research Section A: Accelerators, Spectrometers, Detectors and Associated Equipment*, 592(3):420–427, July 2008. ISSN 0168-9002. doi: 10.1016/j.nima.2008.04.078. URL <https://www.sciencedirect.com/science/article/pii/S0168900208006517>. 5
- [59] S. R. Parnell, A. A. van Well, J. Plomp, R. M. Dalgliesh, N.-J. Steinke, J. F. K. Cooper, N. Geerits, K. E. Steffen, W. M. Snow, and V. O. de Haan. Search for exotic spin-dependent couplings of the neutron with matter using spin-echo based neutron interferometry. *Phys. Rev. D*, 101:122002, Jun 2020. doi: 10.1103/PhysRevD.101.122002. URL <https://link.aps.org/doi/10.1103/PhysRevD.101.122002>. 2
- [60] F. M. Piegsa and G. Pignol. Limits on the axial coupling constant of new light bosons. *Phys. Rev. Lett.*, 108:181801, May 2012. doi: 10.1103/PhysRevLett.108.181801. URL <https://link.aps.org/doi/10.1103/PhysRevLett.108.181801>. 2
- [61] G. Pignol. Probing dark energy models with neutrons. *International Journal of Modern Physics A*, 30(24):1530048, 2015. doi: 10.1142/S0217751X15300483. URL <https://doi.org/10.1142/S0217751X15300483>. 2
- [62] J. S. Plant. Spinwave dispersion curves for yttrium iron garnet. *Journal of Physics C: Solid State Physics*, 10(23):4805, Dec 1977. doi: 10.1088/0022-3719/10/23/014. URL <https://dx.doi.org/10.1088/0022-3719/10/23/014>. 4
- [63] Y. N. Pokotilovski. Limits on short-range spin-dependent forces from spin relaxation of polarized 3He. *Physics Letters B*, 686(2):114–117, 2010. ISSN 0370-2693. doi: <https://doi.org/10.1016/>

- j.physletb.2010.02.014. URL <https://www.sciencedirect.com/science/article/pii/S0370269310001887>. 2
- [64] A. J. Princep, R. A. Ewings, S. Ward, S. Tóth, C. Dubs, D. Prabhakaran, and A. T. Boothroyd. The full magnon spectrum of yttrium iron garnet. *npj Quantum Materials*, 2(1):63, Nov. 2017. ISSN 2397-4648. doi: 10.1038/s41535-017-0067-y. URL <https://doi.org/10.1038/s41535-017-0067-y>. 4
- [65] M. S. Safronova, D. Budker, D. DeMille, D. F. J. Kimball, A. Derevianko, and C. W. Clark. Search for new physics with atoms and molecules. *Rev. Mod. Phys.*, 90:025008, Jun 2018. doi: 10.1103/RevModPhys.90.025008. URL <https://link.aps.org/doi/10.1103/RevModPhys.90.025008>. 2
- [66] A. P. Serebrov. New constraints for CP-violating forces between nucleons in the range 1 micrometer to 1 centimeter. *Physics Letters B*, 680(5):423–427, Oct. 2009. doi: 10.1016/j.physletb.2009.09.025. 2
- [67] S.-i. Shamoto, T. U. Ito, H. Onishi, H. Yamauchi, Y. Inamura, M. Matsuura, M. Akatsu, K. Kodama, A. Nakao, T. Moyoshi, K. Munakata, T. Ohhara, M. Nakamura, S. Ohira-Kawamura, Y. Nemoto, and K. Shibata. Neutron scattering study of yttrium iron garnet. *Phys. Rev. B*, 97:054429, Feb 2018. doi: 10.1103/PhysRevB.97.054429. URL <https://link.aps.org/doi/10.1103/PhysRevB.97.054429>. 4
- [68] I. L. Shapiro. Physical aspects of the space–time torsion. *Physics Reports*, 357(2):113–213, 2002. ISSN 0370-1573. doi: [https://doi.org/10.1016/S0370-1573\(01\)00030-8](https://doi.org/10.1016/S0370-1573(01)00030-8). URL <https://www.sciencedirect.com/science/article/pii/S0370157301000308>. 2
- [69] W. M. Snow, C. Haddock, and B. Heacock. Searches for exotic interactions using neutrons. *Symmetry*, 14(1), 2022. ISSN 2073-8994. doi: 10.3390/sym14010010. URL <https://www.mdpi.com/2073-8994/14/1/10>. 2
- [70] S. Sponar, R. I. P. Sedmik, M. Pitschmann, H. Abele, and Y. Hasegawa. Tests of fundamental quantum mechanics and dark interactions with low-energy neutrons. *Nature Reviews Physics*, 3(5):309–327, May 2021. ISSN 2522-5820. doi: 10.1038/s42254-021-00298-2. URL <https://doi.org/10.1038/s42254-021-00298-2>. 2
- [71] D. Treves. Studies on orthoferrites at the weizmann institute of science. *Journal of Applied Physics no. 36*, 36:1033–1039, 1965. URL <https://doi.org/10.1063/1.1714088>. 3, 11
- [72] V. V. Voronin, V. V. Fedorov, and I. A. Kuznetsov. Neutron diffraction test on spin-dependent short range interaction. *JETP Letters*, 90(1):5–7, Sept. 2009. ISSN 1090-6487. doi: 10.1134/S0021364009130025. URL <https://doi.org/10.1134/S0021364009130025>. 2
- [73] S. Weinberg. Approximate symmetries and pseudo-goldstone bosons. *Phys. Rev. Lett.*, 29:1698–1701, Dec 1972. doi: 10.1103/PhysRevLett.29.1698. URL <https://link.aps.org/doi/10.1103/PhysRevLett.29.1698>. 2
- [74] E. Weisman. *Experimental Searches for Exotic Short-Range Forces Using Mechanical Oscillators*. PhD thesis, Indiana University, Bloomington, Jan. 2017. 3
- [75] H. Yan and W. M. Snow. New limit on possible long-range parity-odd interactions of the neutron from neutron-spin rotation in liquid ^4He . *Phys. Rev. Lett.*, 110:082003, Feb 2013. doi: 10.1103/PhysRevLett.110.082003. URL <https://link.aps.org/doi/10.1103/PhysRevLett.110.082003>. 2
- [76] Y. Zhang and H. Bilheux. URL https://neutrons.ornl.gov/sites/default/files/MARS_Spec_Sheet.pdf. 9